RSC Advances

PAPER

View Article Online
View Journal | View Issue

Cite this: *RSC Adv.*, 2026, **16**, 2179

Self-assembled isomorphous 2D triangular networks: divergent magnetic relaxation in Co(II) and Cu(II)

Luckerman D. G. Botelho, [a] Henrique C. S. Junior, [b] Guilherme P. Guedes, [c] Davor L. Mariano, [d] Angelo M. Gomes, [d] Wallace C. Nunes *[e] and Maria Vanda Marinho *[a]

Two homonuclear coordination networks of general formula $[\{Co(H_2mpba)(dps)\}\cdot 2DMSO]_n$ **(1)** and $[\{Cu(H_2mpba)(dps)\}\cdot 2DMSO\cdot H_2O]_n$ **(2)** [H_4mpba = 1,3-phenylenebis(oxamic) acid; dps = 4,4′-dipyridyl sulfide] were prepared by the diffusion method at room temperature, characterized, and their magnetic properties investigated. The starting 4,4′-dipyridyl disulfide (dpds) ligand undergoes complete *in situ* transformation into dps under mild conditions, affording the two-dimensional polymeric arrays. The H_2mpba^{2-} exhibits the bis-bidentate coordination mode, and the dps serves as a bridging ligand between two metal centers, yielding a two-dimensional coordination network with a triangular-like structure, in which the metal ions act as connecting nodes. AC measurements demonstrate that they exhibit slow magnetic relaxation in the absence of an applied DC field **(1)** and under an applied direct-current (DC) field **(2)**, with a single bottleneck effect. Compound **1** shows a weak but clear out-of-phase signal at zero field, confirming a single-ion magnet (SIM) behavior. At 1 kOe, a bottleneck effect dominates below 7.5 K. At the same time, the Orbach process prevails at 7.5–11.5 K, supported by strong easy-axis anisotropy ($D = -103.7(7)$ cm^{-1}) ($D = -106.0$ cm^{-1} and $|E/D| = 0.23$ from *ab initio* CASSCF/NEVPT2 calculations), and significant rhombicity, yielding an effective energy barrier, $U_{eff} = 56(3)$ K with a pre-exponential factor of relaxation time, $\tau_0 = 1.2(1) \times 10^{-8}$ s. Compound **2** displays field-induced slow relaxation at 1 kOe due to the bottleneck effect.

Received 26th August 2025
Accepted 17th December 2025

DOI: 10.1039/d5ra06376k

rsc.li/rsc-advances

1 Introduction

In the early 2000s, the observation of slow magnetic relaxation in mononuclear rare-earth complexes, most notably the terbium(III) and dysprosium(III) double-decker systems,[1] marked a pivotal moment in the development of molecular nanomagnetism. These compounds, subsequently termed single-ion magnets (SIMs), exhibit strong uniaxial anisotropy and large energy barriers for magnetization reversal (U).[2] A decade later, in 2010, the first SIM based on a 3d transition metal ion, a mononuclear trigonal-pyramidal Fe(II) complex, was reported, underscoring the growing potential of first-row transition metals in the field.[3] Importantly, 3d ions offer several advantages, including the ability to form strongly exchange-coupled spin systems.[4] Moreover, their typically low coordination numbers can minimize ligand-field splitting relative to spin–orbit coupling, thereby enabling slow magnetic relaxation behavior.[4]

With these considerations in mind, the node-and-spacer approach[5] was employed as the central synthetic design strategy. In this context, Co(II) and Cu(II) centers were selected to construct coordination polymers using the sulfur-bridged bipyridyl derivative 4,4′-dipyridyl disulfide (dpds), together with the auxiliary ligand N,N′-1,3-phenylenebis(oxamic acid) (H_4mpba). Co(II) is particularly attractive due to its strong first-order spin–orbit coupling and its noninteger high-spin ground state ($S = 3/2$)[6] (see Table S1, SI, for a concise literature survey of Co(II) compounds that exhibit single-molecule magnets (SMMs) or single-ion magnets (SIMs) behaviors, including magnetic parameters and structural features). The magnetic response follows the thermal population of the Kramers sublevels of the ground term, leading to the characteristic Curie-type behavior ($\chi = C/T$). In addition, second-order spin–orbit coupling between the ground state and low-lying excited states generates a temperature-independent paramagnetism (TIP) contribution. Cu(II), on the other hand, is an $S = 1/2$ for which, in the absence

[a]*Instituto de Química, Universidade Federal de Alfenas, Campus Santa Clara, Alfenas, MG, 37133-840, Brazil. E-mail: maria.marinho@unifal-mg.edu.br*
[b]*Departamento de Química Fundamental, Instituto de Química, Universidade Federal Rural do Rio de Janeiro, Seropédica, RJ, 23890-000, Brazil*
[c]*Instituto de Química, Universidade Federal Fluminense, Niterói, RJ, 24020-141, Brazil*
[d]*Instituto de Física, Universidade Federal do Rio de Janeiro, Cidade Universitária, Rio de Janeiro, RJ, 21941-972, Brazil*
[e]*Instituto de Física, Universidade Federal Fluminense, Niterói, RJ, 24210-346, Brazil, . E-mail: wcnunes@id.uff.br*

of an external field, the electronic states are doubly degenerate ($M_S = \pm 1/2$). This makes Cu(II) systems valuable references for probing anisotropy, exchange pathways, and relaxation dynamics in low-spin molecular magnets.

Beyond the choice of the metal centers, the selection of the spacers is equally important. The ligand 4,4′-dipyridyl disulfide (dpds) is a versatile neutral linker capable of generating one-, two-, or three-dimensional polymeric assemblies (see Tables S2 and S3). This ligand can undergo *in situ* transformation into 4,4′-dipyridyl sulfide (dps), through cleavage of the central S–S bond,[7,8] and the dps ligand is also capable of forming 2D frameworks that help to suppress magnetic interactions between metal-nodes[9,10] (see Tables S4 and S5).

Motivated by the goal of constructing SIM-type coordination polymers in which the spin centers can be well-isolated from each other and the intermolecular magnetic interactions remain negligible, we next incorporated the H_2mpba^{2-} oxamate derivative as a polycarboxylate anionic spacer.[11] This oxamate has been reported in elegant examples of coordination polymers constructed from mixed neutral spacers,[11a,b] and is well known to promote frameworks in which the magnetic centers behave as effectively isolated ions.[12]

Thus, our findings report the first example of M(II)-dps coordination networks incorporating an oxamate derivative that exhibit slow magnetic relaxation. Using the diffusion method, we synthesized and magneto-structurally characterized compounds **1** and **2**. In both systems, the dpds precursor undergoes *in situ* S–S bond cleavage at room temperature, yielding the dps linker. Single-crystal X-ray diffraction reveals that compounds **1–2** form 2D frameworks based on triangular motifs composed of three metal nodes bridged cooperatively by the dps ligand together with an oxamate derivative. The magnetic behavior observed in **1**, supported by theoretical calculations, is fully consistent with its structural features: the large intra- and interlayer metal–metal separations make magnetic exchange between the spin triangles negligible, so that each Co(II) center relaxes essentially as an isolated single-ion unit. Accordingly, compound **1** displays zero-field single-ion magnet (SIM) behavior with slow magnetic relaxation. In contrast, compound **2** exhibits a bottleneck effect at 1 kOe (n = 2.0(1)), indicative of field-induced slow magnetic relaxation. These aspects are discussed in detail below.

2 Experimental section

2.1 Materials

2.1.1 Materials and methods

2.1.1.1. Reagents. Cobalt(II) dichloride hexahydrate (Sigma-Aldrich, 97%), copper(II) dichloride dihydrate (Sigma-Aldrich, 99%), 4,4′-dipyridyldisulfide (or 4-aldrithiol) (Sigma-Aldrich, 99%), and dimethylsulfoxide (DMSO) (Synth) were purchased from commercial sources and used without further purification. The Et_2H_2mpba proligand and K_2H_2mpba were prepared as previously described.[11a,b]

*2.1.1.2. Preparation of **1–2**.* The reactions were carried out without external pH control. The reaction contained equimolar amounts (~0.091 mmol) of the salt (pH ~ 8), H_2mpba^{2-} salt (pH ~ 6), and dpss ligand (pH ~ 7). The stoichiometric combination of the potassium salt K_2H_2mpba and the neutral dpds ligand provided a self-balanced system under diffusion conditions, followed by slow solvent evaporation, as described below:

(1). A DMSO solution (3.0 mL) of dpss (0.020 g, 0.091 mmol) was placed at the bottom of a test tube. Then, a layer of methanol (4 mL) was added, followed by an aqueous solution (3.0 mL) of K_2H_2mpba (0.030 g, 0.091 mmol). A DMSO solution (3.0 mL) of $CoCl_2 \cdot 6H_2O$ (0.020 g, 0.084 mmol) was then carefully layered on top. The tube was sealed with Parafilm® and left to undergo slow diffusion at room temperature. After 25 days, needle-like red crystals were collected by filtration and air-dried. Yield: 54% (0.030 g). IR (cm^{-1}): 3173 (ν_{N-H}); 3059 (ν_{C-H}); 1682 ($\nu_{C=O}$); 1666 (ν_{asCOO}); 1614, 1595, 1586, 1540 ($\nu_{C=C}$); 1482 (ν_{sCOO}); 1412, 1359, 1283 (ν_{CN}); 1044, 944 ($\nu_{S=O}$), and 678 ($\delta_{C-H\ out\text{-}of\text{-}plane}$). Anal. calcd for $C_{24}H_{26}CoN_4O_8S_3$ (653.58 g mol^{-1}): C, 44.06%; H, 4.01%; N, 8.57%; Co, 9.02%. Found: C, 42.94%; H, 3.93%; N, 8.53%; Co, 9.10%.

(2). A DMSO solution (3.0 mL) of dpss (0.020 g, 0.091 mmol) was placed at the bottom of a test tube. Then, a layer of methanol (4 mL) was added, followed by an aqueous solution (3.0 mL) of K_2H_2mpba (0.030 g, 0.091 mmol). A DMSO solution (3.0 mL) of $CuCl_2 \cdot 2H_2O$ (0.020 g, 0.117 mmol) was then carefully layered on top. The tube was covered with Parafilm® and left to diffuse at room temperature. After 3–6 days, a good quantity of green amorphous solid was observed, and the reaction was centrifuged for a few minutes. The remaining mother solution was left undisturbed for approximately two months (~55 days). Needle-like green crystals suitable for X-ray analysis were obtained by slow crystallization, collected by filtration, and air-dried. Yield: 20% (0.015 g). IR (cm^{-1}): 3179 (ν_{NH}), 3098, 2942, 2914, 2862 (ν_{CH}), 1688 ($\nu_{C=O}$); 1654 (ν_{asCOO}); 1608, 1595, 1582, 1531 ($\nu_{C=C}$); 1488 (ν_{sCOO}); 1411, 1356, 1281 (ν_{CN}); 1027, 944 ($\nu_{S=O}$), and 684 ($\delta_{C-H\ out\text{-}of\text{-}plane}$). Anal. calcd for $C_{24}H_{28}CuN_4O_9S_3$ (676.24 g mol^{-1}): C, 42.66%; H, 4.18%; N, 8.30%; Cu, 9.32%. Found: C, 42.42%; H, 4.00%; N, 8.21%; Cu, 12.40%.

2.1.1.3. Physical measurements. IR spectra were recorded using a Thermo Scientific iS50 spectrophotometer (USA) coupled to a Pike Gladi ATR apparatus, covering the wavenumber range 4000–400 cm^{-1} with an average of 144 scans and a spectral resolution of 4 cm^{-1}, using an ATR (attenuated total reflection) apparatus. Elemental analyses were performed using a CHN Elemental Analyzer (PerkinElmer 2400, series II). The elemental composition (%Co in **1** and %Cu in **2**) was determined by ICP-OES (Agilent 5800) using 40 mg of compound **1** and 20 mg of compound **2**. Thermogravimetric analyses (TGA) were conducted with a Netzsch STA 449 F5 Jupiter simultaneous thermal analyzer in the temperature range of 30–1100 °C, using alumina crucibles and approximately 10 mg of the sample. The experiment was carried out under a nitrogen atmosphere at a heating rate of 10 °C min^{-1}. Powder X-ray diffraction data were collected on crushed crystals of **1–2** using a Rigaku Ultima IV with Cu-Kα radiation (λ = 1.5418 Å at 40 kV and 30 mA) and 2θ from 3 to 50°, with a scan rate of 1° min^{-1}, and the step size being 0.02°.

2.1.1.4. Magnetic measurements. Static (dc) magnetic measurements were carried out on polycrystalline samples with

a Cryogenic SQUID magnetometer working in the temperature range 1.8 to 300 K and applied field up to 70 kOe. Dynamic (ac) magnetic susceptibility data were collected with a Quantum Design PPMS using applied dc fields up to 5 kOe in the temperature range 2.0–8.0 K. The experimental susceptibilities were corrected for the diamagnetism of the constituent atoms and the sample holder (a plastic bag).

2.1.1.5. Computational details. To further verify the magnetic anisotropy of **1**, *ab initio* calculations were performed using the ORCA 6.1.0 program package.[13] The all-electron Def2-TZVP basis set[14] was employed for all atoms. The electronic structure of the Co(II) center was modeled using state-averaged complete active space self-consistent field (SA-CASSCF) theory. The active space was constructed from seven electrons in the five 3d-like metal orbitals CAS(7,5). The state averaging incorporated 10 quartet and 40 doublets, and dynamic electron correlation was subsequently included *via* strongly contracted *N*-Electron Valence State Perturbation Theory (SC-NEVPT2).[15] Spin–orbit coupling (SOC) effects were then treated using a quasi-degenerate perturbation theory (QDPT) approach. The resulting spin–orbit states were processed using the SINGLE_-ANISO module[16] to determine the g-tensors, zero-field splitting (ZFS) parameters, and principal magnetic axes.

2.1.1.6. X-ray crystallography. Single-crystal X-ray diffraction data for compounds **1** and **2** were collected on a Bruker D8-Venture equipment using graphite-monochromated Mo-Kα radiation ($\lambda = 0.71073$ Å) at room temperature. Data collection, cell refinement, and data reduction were performed using Bruker Instrument Service vV6.2.16, APEX4,[17] and SAINT V8.40B,[17] respectively. The absorption correction using equivalent reflections was done with the SADABS2016/2 program.[18] The structure solution and full-matrix least-squares refinement based on F^2 were performed with the SHELXS and SHELXL programs.[19] The atoms, except hydrogen, were refined anisotropically. Hydrogen atoms were treated in a mixed refinement. The lattice water hydrogen atoms were not placed in compound **2**. In **1**, two disordered DMSO lattice molecules were refined with two alternative positions, with occupation factors of 0.44621 and 0.55379, and 0.48328 and 0.51679, respectively. For **2**, one disordered DMSO molecule was modeled with two alternative positions, affording occupancy factors of 0.43359 and 0.56641, while the second one occupies three different sites with chemical occupancies of 0.26032, 0.36953, and 0.37014. Structure drawings were made by the Mercury program.[20] Crystal data and details of the data collection and refinement for **1–2** are listed in Table 1. The crystallographic data are available in the SI section as CIF files. CCDC numbers are 2469011 and 2469012.

Table 1 Crystal data and structure refinement details for compounds **1–2**

Compound	**1**	**2**
Chemical formula	$C_{24}H_{26}CoN_4O_8S_3$	$C_{24}H_{28}CuN_4O_9S_3$
Fw/g mol^{-1}	653.58	676.24
Temperature/K	293	293
Crystal system	Monoclinic	Monoclinic
Space group	*C*2/*c*	*C*2/*c*
Z	8	8
λ/Å	0.71073	0.71073
a/Å	16.7517(7)	16.6448(8)
b/Å	10.2858(4)	10.3055(5)
c/Å	34.5008(16)	34.8408(16)
β/°	100.862(2)	101.442(2)
V/Å^3	5838.1(4)	5857.6(5)
Crystal size/mm	0.14 × 0.10× 0.04	0.37 × 0.17 × 0.10
ρ_{calc}/g cm^{-3}	1.487	1.529
μ mm^{-1}	0.86	1.02
Θ range/°	2.4–25.7	2.3–26.4
Data collected	40 716	47 956
Independent reflections	5156	5171
Reflections ($I > 2\sigma(I)$)	4094	4519
R_{int}	0.069	0.041
F(000)	2696	2776
Refined parameters	373	374
Goodness-of-fit on F^2	1.15	1.03
R [$F^2 > 2\sigma(F^2)$]	0.087	0.059
wR (F^2)[a,b]	0.194	0.165
Largest diff. Peak/hole/e Å^{-3}	1.49/−0.73	1.04/−0.91
CCDC deposit number	2469011	2469012

3 Results and discussion

3.1 General characterization (CHN, ICP-OES, IR, thermal, and PXRD analyses)

The CHN elemental analysis and ICP-OES values are consistent with the proposed molecular formula. For compound **2**, a better agreement (lower deviation) was observed when the calculation was based on the solvent-free composition, which yielded the smallest error in the ICP-OES results. However, X-ray diffraction and TGA analyses confirmed the presence of DMSO and water molecules in the crystal lattice of **2**.

The IR spectra of **1–2** are shown in Fig. S1. The spectra show the occurrence of one band assigned to $\nu_{as}(COO^-)$ at 1668 (**1**) and 1654 (**2**) cm^{-1} and one band assigned to $\nu_s(COO^-)$ at 1483 (**1**) and 1488 (**2**) cm^{-1}, which may be related to the presence of the H_2mpba^{2-} ligand. The band assigned to $\nu(C{=}O_{amide})$ occurs at 1682 (**1**) and 1688 cm^{-1} (**2**), and the absorption peaks at 1614 (**1**) and 1608 (**2**) cm^{-1} were attributed to ν(CC) stretching vibrations.[21] The IR spectra also reveal N–H stretching at 3173 (**1**) and 3179 (**2**) cm^{-1}, supporting the H_2mpba^{2-} partial deprotonation form.[11a,b,11d,12g,22] Additional peaks were observed in the IR spectra due to the presence of the dps ligand. The set of absorptions assigned to this ligand [~1595 and 1582 cm^{-1}, attributed to $\nu_{C=C}$ and $\nu_{C=N}$] for compounds **1** and **2** supports a bridging coordination mode towards Co^{II} (**1**) and Cu^{II} (**2**) ions. This is evident from the shift to higher wavenumbers compared to the main peak at 1568 cm^{-1} in the free ligand.[10,23] The peaks at 1040 and 1027 cm^{-1} can be assigned to the stretching vibrations (ν_{SO}) for the DMSO molecule.[24] Thermogravimetric analyses (TGA) of compounds **1** and **2** (Fig. S2) revealed similar thermal behavior. Both compounds exhibited minimal mass loss in the 30–75 °C range, accounting for approximately 2.0% of the total mass for compound **1** and 2.1% for compound **2**. The initial weight losses occur up to the temperature of 320 °C for compounds **1** and **2**, specifically, two DMSO molecules in compound **1**, and two DMSO molecules along with one water

molecule in compound **2**, as well as the loss of the dps ligand (obsd. 51.7%, calcd. 52.6% for **(1)**; obsd. 53.1%, calcd. 53.6% for **(2)**). A third weight loss is observed shortly after these initial losses, likely due to the partial decomposition of the H_2mpba^{2-} ligand into phenylene(oxamate) **(1)** and the total decomposition **(2)**, occurring at approximately 900 °C (obsd. 26.2%, calcd. 25.0% for **(1)**; obsd. 33.1%, calcd. 36.0% for **(2)**). The final mass loss residues could tentatively be attributed to $CoCO_3$ (calcd. 18.2%) **(1)** and CuO (calcd. 11.9%) **(2)**.

The experimental and calculated powder X-ray diffraction (PXRD) patterns (Fig. S3 **(1)** and S4 **(2)**) agree well with each other, confirming the good phase purity of the crystalline powder samples of each compound.

3.1.1 Description of the structure. Single-crystal X-ray diffraction revealed that compounds **1** and **2** are isomorphic, crystallizing in the monoclinic *C*2/*c* space group. Data collection, crystal data, and refinement parameters are summarized in Table 1. Their chemical compositions are slightly different due to the metal ion and one additional lattice water molecule in **2**, both compounds present the same structural arrangement. A generic fragment of the crystal structure of **1** and **2** is depicted in Fig. 1.

It comprises one independent partially deprotonated H_2mpba^{2-} and one independent dps ligand bridging two different metal ions M1 and $M1^{iii}$ or M1 and $M1^{iv}$. Selected bond lengths are listed in Table S6.

Due to the symmetrical operations of the *C*2/*c* space group, the metal ion coordination sphere is further filled with additional bidentate H_2mpba^{2-} and dps ligands, leading to a 2D array as shown in Fig. 2.

This polymeric arrangement affords triangular-like channels along the bc crystallographic plane in which the metal ions act as a node. In both compounds, these channels are filled with two DMSO (**1**) or two DMSO and one water (**2**) molecule. Each metal ion is coordinated by four oxygen atoms from two different H_2mpba^{2-} and two pyridyl nitrogen atoms from two dps ligands, forming a distorted octahedral geometry. In both compounds, the H_2mpba^{2-} ligand acts as a bridging ligand, a μ-κ^2O,O′:κ^2O″,O‴coordination mode, while the dps ligand adopts a μ-κN:κN′ bridging coordination mode. Three oxygen atoms (O1, O2, and $O5^i$) and one nitrogen atom (N3) coordinate to the equatorial sites of the metal ion, while the axial positions are filled by the remaining H_2mpba^{2-} oxygen ($O6^i$) and dps nitrogen ($N4^{ii}$) atoms.

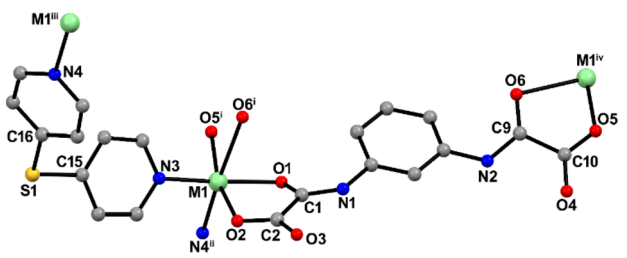

Fig. 1 Fragment of **1** (M = Co) and **2** (M = Cu) crystal structure. Hydrogen atoms and lattice molecules have been omitted for the sake of clarity. Symmetry operation to generate equivalent atoms: (i) 3/2 − *x*, *y* + 1/2, 1/2 − *z*; (ii) *x*, *y* + 1, *z*; (iii) *x*, *y* − 1, *z*; (iv) 3/2 − *x*, *y* − 1/2, *z* − 1/2 (for **1**); (i) 3/2 − *x*, *y* + 1/2, 3/2 − *z*; (ii) *x*, *y* − 1, *z*; (iii) *x*, *y* + 1, *z*; (iv) 3/2 − *x*, *y* − 1/2, 3/2 − *z* (for **2**).

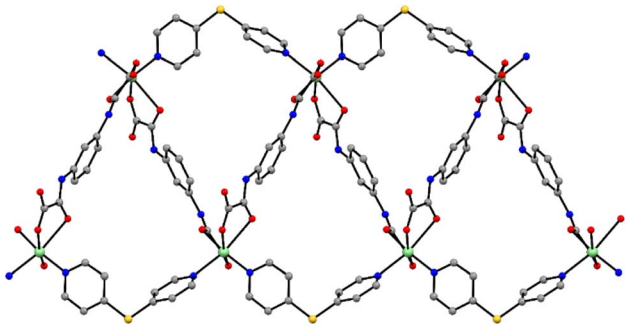

Fig. 2 2D polymeric arrangement of **1** and **2**. Lattice DMSO and water molecules and hydrogen atoms were omitted for clarity. Color codes: green = cobalt(II) or copper(II), gray = carbon, red = oxygen, blue = nitrogen, and yellow = sulfur.

The M1–O and M1–N distances range from 2.048(3)–2.218(4) Å in **1**, and from 1.977(3)–2.499(3) Å in **2**. Due to the Jahn-Teller distortion expected for d^9 ions, the M1–$O6^i$ and M1–$N4^{ii}$ bond lengths in **2** are larger than those forming the equatorial plane. The bond lengths for cobalt(II) and copper(II) derivatives are in the typical range found in the literature.[11e,12g,25–27] The bond angles between the metal ions and ligand donor atoms fall within the ranges 77.4(2)° to 98.6(2)° for **1**, and 74.1(1)° to 98.2(1)° for **2**. These values indicate a significantly distorted hexacoordinated environment for both complexes, as they deviated considerably from the ideal 90° angles characteristic of the octahedral geometry. Furthermore, to evaluate the distortion of the coordination environment around the Co^{II} and Cu^{II} ions, the continuous shape measure (CShM) parameters for **1–2** were calculated using the Shape 2.1 program.[28] As shown in Table S7, although the coordination geometries of **1–2** can still be described as an octahedron, the deviation from the ideal Oh octahedron (for ideal Oh symmetry, CShM = 0) is significant, with the CShM values of 16.441 **(1)** and 17.359 **(2)**.

In the dps moiety, the C15–S1–C16 bond angle in both complexes is *c.a.* 101°, which plays an important role in the 2D structural arrangement, since dps is a rigid ligand connecting two metal ions. Moreover, the dps phenyl rings are twisted by 71° and 68°, respectively, for **1** and **2**. Concerning the H_2mpba^{2-} ligands, the coordinating oxamate group planes are *c.a.* 46° for both complexes. In addition, C1–N1–C3 and C7–N2–C9 bond angles also revealed a very similar structural arrangement for **1** and **2**.

In the triangular-like motifs seen in the 2D array, two different distances between the metal centres are present, namely M1⋯$M1^{iii}$ and M1⋯$M1^{iv}$. The first one is mediated by dps ligands, and it is the shortest one, with values of 10.286(1) Å (for **1**) and 10.3055(8) Å (for **2**). The largest distances of 12.097(1) Å (**1**) and 12.142(1) Å (**2**) were seen when H_2mpba^{2-} bridges the metal ions. The M⋯M distances through bridging dps ligand observed in the polymeric chains of **1** and **2** are comparable to those reported in the literature for first-row transition metal

Table 2 Selected polymeric chains involving the dps (from *in situ* cleavage–reorganization of the dpss ligand) and the H_2mpba^{2-} bridging ligands, and the **1–2** networks[a]

Compound	Methodology	Metal	M···M (Å)	Database identifier	Ref.
dps bridges					
$\{[Co(dps)_2(SeCN)_2]\cdot H_2O\}_n$	Diffusion	Co(II)	10.175(3)	WIZLEY	7
$[Co_2(dps)_2(5\text{-Br-Hip})_4]_n$	Solvothermal. (170 °C – 3 days)	Co(II)	10.224	QIJSIN	29
$[Fe(NCS)_2(dps)_2]\cdot 2H_2O$	Stirring (at room temperature)	Fe(II)	10.288	IREBEN01	8
$[Zn(NCO)_2(dps)]$	Stirring (at room temperature)	Zn(II)	10.714(2)	LOHROR	8
[Zn(muco)(dps)]	Solvothermal (100 °C – 4 days)	Zn(II)	10.878	JUFLED	21
$[Co_2(dps)_2(CH_3O\text{-ip})_2]_n$	Solvothermal (160°C – 3 days)	Co(II)	11.158(6)	HOMGUN	30
$[Co_2(^i PrIPA)_2(dps)]_n$	Solvothermal (120 °C – 3 days)	Co(II)	10.1870(9)	NUWFOD	31
$[Co_3(^i BuOIPA)_3(dps)(H_2O)]_n$	Solvothermal (120 °C – 3 days)	Co(II)	9.8429(2)	NUWFIX	31
H_2mpba^{2-} bridges					
[Cu(bipy)(H_2mpba)]·dmso	Diffusion	Cu(II)	7.0263(14)	QIQYUM	11*e*
$[Co_2(H_2mpba)_2(H_2O)_4]_n\cdot 4nH_2O$	Stirring (at room temperature)	Co(II)	12.195(6)	UYIQEB	11*b*
$[Co_2(H_2mpba)_2(CH_3OH)_2(H_2O)_2]_n\cdot 0.5nH_2O\cdot 2n$dpss	Stirring (at room temperature)	Co(II)	5.121(3)	UYIQIF	11*b*
H_2mpba^{2-} and dps bridges					
$[\{Co(H_2mpba)(dps)\}\cdot 2DMSO]_n$	Diffusion (at room temperature)	Co(II)	10.286(1)/12.097(1)	—	This work
$[\{Cu(H_2mpba)(dps)\}\cdot 2DMSO\cdot H_2O]_n$	Diffusion (at room temperature)	Cu(II)	10.3055(8)/12.142(1)	—	This work

[a] Abbreviations: 5-Br-H_2ip = 5-bromoisophthalate, muco = trans, *trans*-muconate dianion, CH_3O–H_2ip = 5-methoxyisophthalate, iPrIPA = 5-i-propoxyisophthalate, iBuOIPA = 5-i-butoxyisophthalate, bipy = 2,2′-bipyridine, dpss = 2,2′-dipyridyldisulfide.

polymeric chains, particularly those where dps was generated *in situ* from dpss (see Table 2). Although comparisons are limited due to the scarcity of polymeric chains involving the H_2mpba^{2-} ligand, it is noteworthy that the M···M distances in **1** and **2** resemble those of the linear cobalt(II) chain $[Co_2(H_2mpba)_2(H_2O)_4]_n\cdot 4nH_2O$.[11*b*] The M···M distance in **2** is significantly longer than that observed in the linear copper(II) chain [Cu(bipy)(H_2mpba)]·DMSO,[11*e*] possibly due to the bidentate coordination mode of the 2,2′-bipyridine ligand.

Finally, to close the triangular-like unit, the $M1^{iii}\cdots M1^{iv}$ distances are the same for $M1\cdots M1^{iv}$ since the connection between the two metal centres is also made by a H_2mpba^{2-} ligand. Compound **2** shows slightly larger metal…metal distances than **1**. It is important to note that both bridging ligands generate similar 2D layers in **1–2**. When separated by dps or H_2mpba^{2-} ligands, the M^{II} ions within each triangular unit are well-isolated.

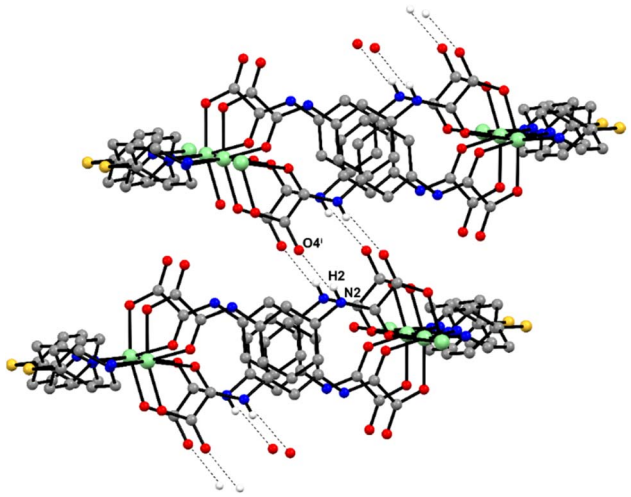

Fig. 3 Intermolecular interactions involving oxamate motifs connecting the 2D sheets in the solid state for **2**. Symmetry operation to generate equivalent atom: $i = 2 - x, +y, 3/2 - z$.

The crystal packing of complexes **1** and **2** is stabilized by a hydrogen-bonding network involving the oxamate group (N–H···$O_{oxamate}$), as well as interactions between the oxamate units and lattice DMSO molecules (N–H···O_{dmso}). The former interaction plays a crucial role in the molecular architecture of the solid state, which connects the sheets, as illustrated in Fig. 3 for the copper-based network. The crystal packing of complexes **1** and **2** is further stabilized by short contacts of type C_{sp2}–H···C_{sp2} and C_{sp3}–H···C_{sp2} involving aromatic rings, the oxamate group, and DMSO molecules.

3.1.2 Magnetic properties. The dc magnetic properties of compound **1**, in the form of $\chi_M T$ product against T and M *vs.* H/T plots (χ_M is the magnetic susceptibility per cobalt(II) ion), are shown in Fig. 4.

At room temperature, χT was 3.6 $cm^3\ mol^{-1}$ K, significantly higher than the expected spin-only value of 1.875 $cm^3\ mol^{-1}$ K for an isolated Co(II) ion ($S = 3/2$, $g = 2.0$). This indicates the presence of considerable orbital angular momentum contributions. Upon cooling, the values of χT steadily decreased to 2.2 $cm^3\ mol^{-1}$ K at 2 K. No abrupt variation in χT *vs.* T was observed at low temperatures, indicating very weak intermolecular interactions present in compound **1**. The continuous decrease of χT from room temperature is primarily attributed to thermal depopulation of the energy levels of the $S = 3/2$ Co ions, resulting from the zero-field splitting effects. The non-superposition of the reduced magnetization curves in *m vs.* H/

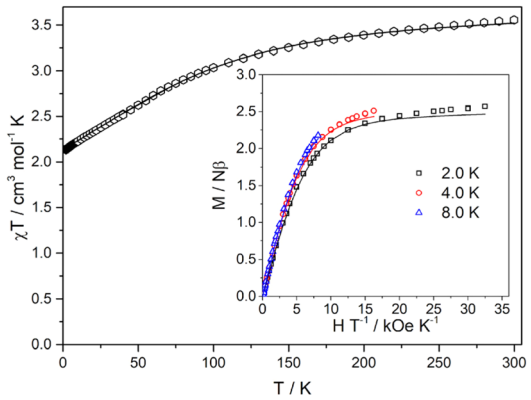

Fig. 4 Temperature dependence of the χT product for **1** measured in the applied field of 1 kOe: (symbols) experimental; (lines) best-fit curve through eqn (1) (see text). Inset: experimental magnetization *vs.* reduced field at different temperatures for **1** at 2, 4, and 8.0 K.

T plots (inset of Fig. 4) indicates magnetic anisotropy, supporting the presence of significant zero-field splitting in this complex. To further investigate the magnetic anisotropy of the Co(II) ion, both the χT value and the magnetization data were fitted using the spin Hamiltonian containing ZFS and Zeeman effect (eqn (1)):

$$\hat{H} = D\left(\hat{S}z^2 - \frac{S(S+1)}{3}\right) + E\left(\hat{S}x^2 - \hat{S}y^2\right) + \mu_B \vec{\hat{S}}\cdot\hat{g}\cdot\vec{H} \quad (1)$$

D and E represent axial and rhombic ZFS parameters, respectively, μ_B is the Bohr magneton, $\hat{S}$ is the spin operator, and $\vec{H}$ is the magnetic field vector, implemented in the PHI program.[32] The best fit parameters are $D = -103.7(7)$ cm^{-1}, $E = 1.14(7)$ cm^{-1}, $g_{eff} = 2.772(1)$ and $zJ = -0.005(1)$ cm^{-1}. The zJ term was introduced to account for possible intermolecular interactions and is defined as $\chi'_M = \chi_M/[1 - (zJ/Ng^2\mu_b^2)\chi_M]$.- These results indicate a significant easy-axis magnetic anisotropy for **(1)** with a slight deviation from axial symmetry due to the structural distortion of the field around the Co(II) ion. In contrast to the majority of cobalt(II) systems investigated as single-molecule magnets (see Table S1), which predominantly exhibit a positive D value,[9,33–35] our results reveal that compound **1** displays a large negative D parameter of 103.7(7) cm^{-1}. Similar behavior indicating easy-axis magnetic anisotropy, as suggested by negative D values, has previously been reported for a number of other Co^{II} complexes[36–39] (see Table S1).

To further verify the magnetic anisotropy of **1**, *ab initio* CASSCF/NEVPT2 calculations were performed, and the SINGLE_ANISO analysis confirms that the Co(II) center in **1** is a high-spin ($S = 3/2$) system with strong easy-axis magnetic anisotropy. Analysis of the ground doublet within the lowest four spin–orbit states yields an axial ZFS parameter $D \sim -106.0$ cm^{-1}, which is quite close to the fitted experimental value. This splitting sets a large theoretical thermal barrier $U_{eff} = 228.1$ cm^{-1}, which is based on the *ab initio* energy of the first excited Kramers doublet.

However, the large U_{eff} barrier is effectively short-circuited by a substantial rhombic ZFS parameter $E = -24.3$ cm^{-1}. The resulting rhombicity ratio, $|E/D| \sim 0.23$, is about 69% of the theoretical maximum 1/3. Such strong rhombicity induces significant quantum-mechanical mixing between the ground $M_S = \pm 3/2$ and excited $M_S = \pm 1/2$ states, opening an efficient QTM pathway at zero field and consequently suggesting that this complex is a field-induced single-ion magnet.

Evidence for this dominant QTM channel is explicit in the computational data. A pure, unmixed $M_s = \pm 3/2$ ground state in the limit $E = 0$ would be essentially "EPR-silent" in the transverse plane, requiring $g_X = g_Y = 0$. In contrast, the calculated effective g tensor for the ground Kramers doublet is highly anisotropic, with a very large easy-axis component $g_Z \sim 8.61$ (derived from $2 \times |\langle M_Z \rangle|$) and clearly non-zero transverse components g_X and g_Y. The non-zero E term and the large off-diagonal crystal-field parameters B(2, ±1) and B(2, ±2) quantify the state mixing that generates these transverse g values (Fig. S5 and Tables S8–S14).

For compound **2**, the χT product, which is 0.47 cm^3 mol^{-1} K at room temperature, continuously decreases until around 4 K, when the decrease becomes a little steeper, reaching 0.43 cm^3 mol^{-1} K at 2 K (Fig. 5). The expected value for Cu^{2+} ions at room temperature is 0.38 cm^3 mol^{-1} K, considering a free Cu^{2+} ion state ($S = 1/2$, $g = 2$). The analysis of the χT *vs.* T magnetic data was performed using the Curie law (eqn (2)):

$$\chi_M = \frac{Ng^2\mu_b{}^2 S(S+1)}{3kT} + \text{TIP} \quad (2)$$

modified to account for weak intermolecular interactions (zJ'), eqn (3):

$$\chi = \frac{\chi_M}{1 - \left(\frac{zJ'}{Ng^2\mu_b{}^2}\right)\chi_M} \quad (3)$$

where g is the spectroscopic splitting factor, N is Avogadro's number temperature-independent paramagnetism, and $S = 1/2$ for the Cu(II) ion. Simultaneous fitting of the data $\chi_T(T)$ and magnetization data was performed using the PHI program, employing the equation $M(H) = Ng\mu_b SB_S\left(\frac{g\mu_{bSH}}{kT}\right)$, where B_S is

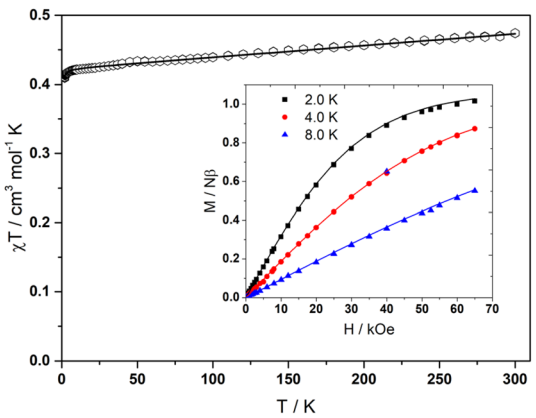

Fig. 5 Temperature dependence of the χT product for **2** measured in the applied field of 1 kOe: (symbols) experimental; (lines) best-fit curve through eqn (2) (see text). Inset: experimental magnetization *vs.* magnetic field at different temperatures for **2** at 2.0, 4.0, and 8.0 K.

the Brillouin function. The best agreement with the experimental data for **2** was obtained with $g = 2.129$, $zJ' = -0.03$ cm^{-1}, TIP $= 1.7 \times 10^{-4}$ cm^3 mol^{-1}. The temperature-independent paramagnetic term agrees with typical values,[40] and the small zJ' value indicates the weak intermolecular interactions. The observed magnetic behavior for **1** is consistent with the structural data, as significant intra- and interlayer metal–metal distances suggest any magnetic coupling between the spin triangles would be very weak.

3.1.3 Dynamic (ac) magnetic measurements. To explore the magnetization dynamics and to investigate possible slow magnetic relaxation in compounds **1** and **2**, alternating current (ac) susceptibility was measured over a frequency range of 0.1 to 10 kHz and an applied field range of 0.0 to 5.0 kOe. For complex **1**, in the absence of an applied dc field, a weak but significant signal of the out-of-phase (χ''_M) component of ac susceptibility was observed. This suggests that **1** is a single-ion magnet (see Fig. S6a). The Cole–Cole plot is tightly centered on the maxima at different temperatures, indicating a single magnetic relaxation process (Fig. S6b). Fig. 6(a) shows the frequency dependence of the in-phase (χ'_M) and the out-of-phase (χ''_M) susceptibility of **1** measured under an applied dc field of 1 kOe. Both components show significantly increased magnitude at 1 kOe, which is consistent with suppression of the Quantum Tunneling of Magnetization (QTM) process. For compound **2**, χ''_M shows no frequency dependence in measurements at zero applied field. However, χ''_M displays a frequency-dependent behavior under 1 kOe, as shown in Fig. 6(b). These results indicate that **2** exhibits field-induced slow magnetic relaxation. The χ'_M and χ''_M data were analyzed using the generalized Debye model with CC-FIT2 software,[41] furnishing the relaxation time (τ) at different temperatures, the parameter characterizing the width of the relaxation time distribution (α), and other parameters presented in Tables S15–S17.[42]

Fig. 7(a) shows the Cole–Cole plot obtained for **1** measured under 1 kOe. The Cole–Cole plot displays semicircles and symmetrical shapes, with α in the range 0.89–0.13, which is a moderate distribution of relaxation times. Fig. 7(b) shows the Cole–Cole plot of **2**, which is more narrow on the maxima at different temperatures, with α in the range 0.20–0.03, suggesting a single relaxation magnetic process.

The relaxation temperature dependence has been analyzed through different models, the best simulation being achieved by eqn (4):

$$\tau^{-1} = CT^n + \tau_0^{-1}\exp\left(\frac{-U_{eff}}{kT}\right) \quad (4)$$

where the first and second terms account for the Raman and Orbach processes, respectively.[43] These processes are defined by

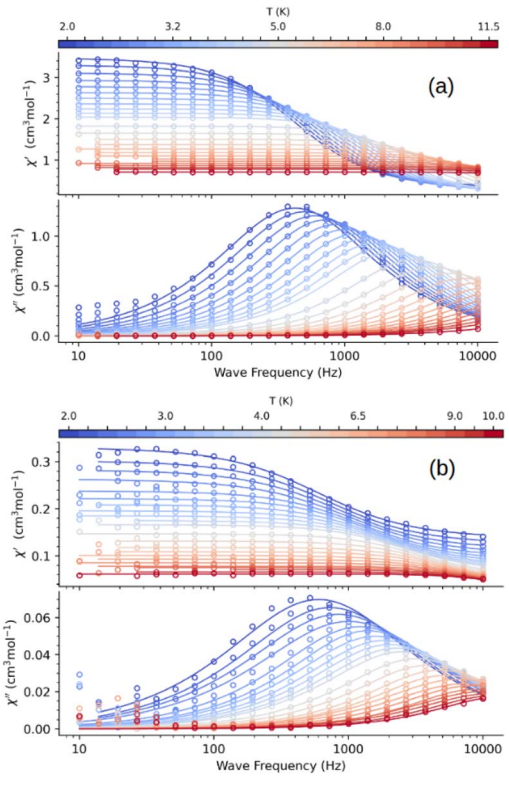

Fig. 6 Real (χ') and imaginary (χ'') components of the magnetic susceptibility measured under an applied field of 1.0 kOe and a frequency range of 0.1–10 kHz for **1** (a) and **2** (b). The solid lines represent the best-fit curves using the parameters from the generalized Debye model.

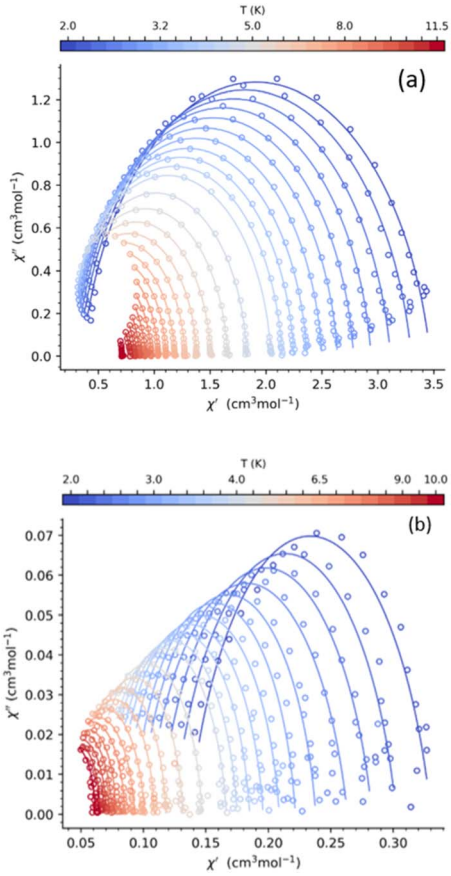

Fig. 7 Cole–Cole plot obtained from the frequency-dependence of the ac susceptibility measured at 1 kOe for **1** (a) and **2** (b). Lines represent the best-fit curves obtained using a generalized Debye model according to the description in the text.

the Raman coefficient (C) and the exponent (n), and by the Orbach effective energy barrier for the relaxation of the magnetization (U_{eff}) and the pre-exponential factor (τ_0), respectively. The Orbach process involves phonon absorption followed by emission, resulting in relaxation *via* a real excited state. In contrast, the Raman process proceeds through a virtual state.[44]

The relaxation time as a function of temperature (Arrhenius plot) for **1** and **2**, obtained under a dc applied field of 1 kOe, is shown in Fig. 8(a) and (b), respectively. The data for **1** under a zero dc applied field is shown in Fig. S7. At zero applied field, the best fit of eqn (4) for **1** was a single Raman process, but with an exponent n lower than the expected range for that mechanism.

These exponent values are also higher than those of the direct process ($\tau \propto T^{-1}$) but fall within the expected range for the bottleneck effect, which has an exponent of approximately 2. The bottleneck effect arises from hindered energy transfer between magnetic spins and surrounding phonons. This results in the reabsorption of energy from the lattice phonons back to the spins, which leads to a slow relaxation time. The slow magnetic relaxation associated with the bottleneck effect occurs due to the interaction between the spin system and the environment lattice, and when conventional relaxation mechanisms, such as thermally activated processes (over-barrier) or quantum tunneling, are suppressed. For the spins in a system to relax from an excited state to the ground state, they must release their excess energy. This energy is dissipated into the system through Crystal lattice vibrations, resulting in the emission of phonons. The slow magnetic relaxation of the spin-phonon bottleneck occurs when the energy released by the relaxing spins cannot be dissipated into the thermal reservoir at a sufficiently rate. This causes the spin system and the lattice to be out of thermal equilibrium. In this regime, the relaxation time is expected to follow the relationship $\tau \propto T^{-2}$.[11c,43]

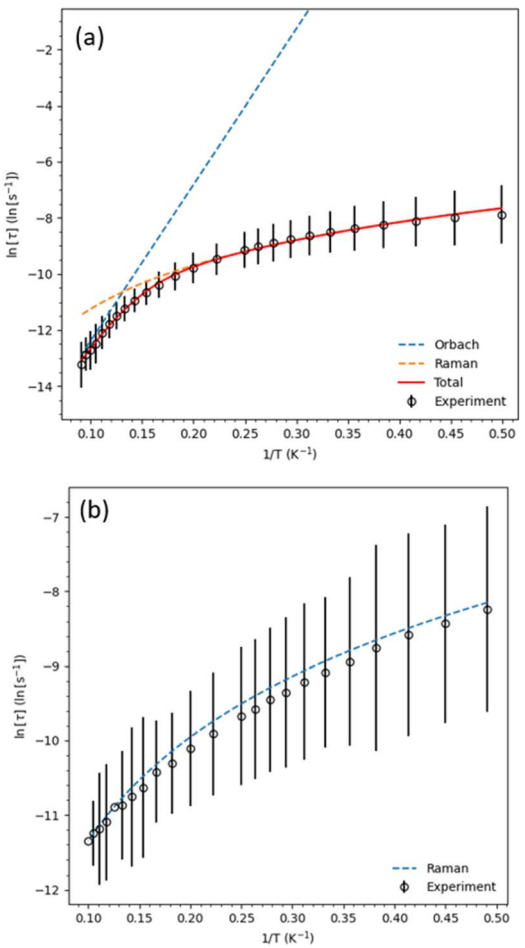

Fig. 8 Arrhenius plots obtained from the ac susceptibility measured under 1 kOe for **1** (a) and **2** (b). Lines represent the best-fit curves obtained using eqn (4) according to the description in the text.

However, exponent n slightly lower or higher than 2.0 has been observed in various compounds, depending on the values of the applied dc field.[11c,45] This suggests a bottleneck effect may occur for **1** at zero applied field (see Table 3).[11c,40] Although *ab initio* calculations suggested that **1** would exhibit efficient quantum tunneling, we observed a bottleneck effect in this compound in the absence of a dc field. We attribute this effect to molecular interactions affecting the energy levels of this compound.

For 1 kOe, the best-fit of eqn (4) to the Arrhenius plot of **1** was the Raman again with temperature exponent n close to the values found for bottleneck effect dominating the relaxation at temperatures lower than 7.5 K. The Orbach process dominates the relaxation in temperatures between 7.5–11.5 K. These values are within the range typically observed for Co single-ion magnets.[11c,46,47] For complex **2**, the magnetic relaxation is well described by the Raman process, but with the exponent value consistent with the bottleneck effect[18] (see Table 3). The structural and magnetic behavior observed for both compounds **1** and **2** indicates that they behave as mononuclear species with high anisotropy.

The magnetic relaxation behavior observed for **1** (a bottleneck at zero field and a bottleneck plus Orbach processes at 1 kOe) is consistent with the strong easy-axis anisotropy ($D = -103.7(7)$ cm^{-1}) and significant rhombicity found for the Co(II) ion from the χT *vs.* T analysis. The high rhombicity facilitates the direct relaxation, while structural distortion increases mode density, yielding a bottleneck effect. The large anisotropy provides the excited states necessary for the Orbach process. On the other hand, in compound **2**, the Cu(II) is a $S = 1/2$ Kramers ion that has a single Kramers doublet as its ground state; therefore, there are no real excited states necessary for the Orbach mechanism. In addition, the weak magnetic

Table 3 Dynamic magnetic parameters for **1** and **2**

Compound	Parameter	0.0 (kOe)	1.0 (kOe)
1	C ($s^{-1}K^{-n}$)	3.21(12)	2.66(5)
	n	1.38(14)	2.2(1)
	τ_0 (s)	—	$1.2(1) \times 10^{-8}$
	U_{eff}/K_B (K)	—	56.3
2	C ($s^{-1}K^{-n}$)	—	2.9(1)
	n	—	2.0(2)

interactions between Cu ions prevent the spin–spin cross-relaxation pathway, weakening the Direct process. The bottleneck occurs for this complex under an applied field of 1 kOe. In this case, transitions within the ground Kramers doublet proceed *via* slow phonon-mediated pathways, as the doublet is split by the applied magnetic field. However, since the number of phonons potentially involved in a two-phonon Raman pathway is much higher than in a direct process or bottleneck effect, and given the expected exponent values for the Raman process ($n = 6$–9), this mechanism should dominate relaxation, particularly at slightly higher temperatures.[44] However, we observed only a bottleneck. Nevertheless, we observed only a bottleneck effect for **2** in the temperature range 2 to 10 K. The reason the Raman process is not observed for compounds **1** and **2** likely arises from the vibrational properties of their ligands, which will be investigated in detail in future work.

4 Conclusion

In conclusion, we report the first M^{II}–dps–oxamate two-dimensional coordination networks, with Co(II) and Cu(II) compounds displaying single-ion magnet (SIM) properties. The starting 4,4′-dipyridyl disulfide (dpds) ligand was fully converted into 4,4′-dipyridyl sulfide (dps) through an *in situ* rearrangement at room temperature using the diffusion method. The solid-state characterization (elemental analysis, ICP-OES, IR spectra, TG analysis, single-crystal X-ray diffraction, and Powder X-ray diffraction), together with the magnetic measurements and theoretical calculations, are all in full agreement. The phase purity of **1** and **2** was confirmed by comparing the experimental PXRD patterns with those calculated from the single-crystal structures. The 2-D polymeric arrangement was examined by SCXRD, affording triangular-like channels in which the metal ions act as a node. To close the triangular-like unit, two metal centres are connected by one dps ligand, and the third one by the H_2mpba^{2-} ligand, with the M^{II} ions within each triangular unit well-isolated. The detailed study of the dynamic susceptibilities revealed that the compounds behave as mononuclear species exhibiting slow magnetic relaxation in the absence of an applied DC field **(1)** and under an applied direct-current (DC) field **(2)**. For **1**, a weak but significant out-of-phase signal is observed at zero field, indicating single-ion magnet (SIM) behavior. At 1 kOe, the bottleneck effect dominates at temperatures below 7.5 K, while the Orbach mechanism prevails in the higher temperature range of 7.5–11.5 K, supported by strong easy-axis anisotropy ($D = -103.7(7)$ cm^{-1}) and significant rhombicity, yielding an effective energy barrier of $U_{eff} = 56.3(2)$ K with a pre-exponential factor $\tau_0 = 1.2(1) \times 10^{-8}$ s. For compound **2**, the Cu(II) ion ($S = 1/2$) exhibits field-induced slow magnetic relaxation attributed to a bottleneck effect at 1 kOe ($n = 2.0(1)$, $C = 2.9(1)$ s^{-1} K^{-2}), as no real excited states are available for the Orbach process and the weak magnetic coupling prevents spin–spin cross-relaxation, weakening the Direct process. The theoretical calculations have shown **1** to possess a large, negative D value of -106.0 cm^{-1}, which is quite close to the fitted experimental value ($D = -103.7$ (7)), confirming the strong easy-axis magnetic anisotropy. The theoretical results allowed us to assign an E/D value to the cobalt(II) center in **1**, revealing the presence of a strong in-axis anisotropy $|E/D| \sim 0.23$. Despite the quantum tunneling predicted by theoretical calculations, the bottleneck effect in **1** likely results from weak intermolecular interactions.

Author contributions

All authors contributed to the writing of the manuscript and approved the final version. L. D. G. B. synthesized and characterized the system by infrared spectroscopy, thermal analysis, and Powder X-ray diffraction; G. P. G. collected/treated single-crystal X-ray diffraction data; A. M. G, D. L. M, and W. C. N. collected and performed the magnetic data acquisition and processing; H. C. S. Jr. performed and analyzed the theoretical calculations; M.V.M. participated in supervising the synthesis, all analyses, and interpretation, besides writing and reviewing all the data of the paper. All authors contributed to the writing – original draft and to the review & editing of the manuscript.

Conflicts of interest

The authors declare no competing financial interest.

Data availability

The authors confirm that the data supporting the findings of this study are available within the article and its supplementary information (SI). Supplementary information: revision (dps and dpss) based compounds. FTIR spectra, TG curves, PXRD patterns, and magnetic data. Cobalt(II) and copper(II) SIMs/SMMs from literature survey (Table S1); Revision (dps and dpss) based compounds (Tables S2–S5); Selected bond distances (Table S6); CShM parameters (Table S7); *Ab initio* calculation data (Tables S8–S14); Magnetic data (Tables S15–S17). FTIR spectra (Fig. S1), TG curves (Fig. S2), PXRD patterns (Fig. S3 and S4), and magnetic data (Fig. S5–S7). See DOI: https://doi.org/10.1039/d5ra06376k.

CCDC 2469011 and 2469012 contain the supplementary crystallographic data for this paper (**1** and **2**).[48a,b]

Acknowledgements

M. V. M. dedicates this work to the memory of her invaluable friend, Prof. Miguel Julve, whose brilliant academic career was marked by significant contributions to the chemistry of oxamate ligands and derivatives. M. V. M. thanks the Fundação de Amparo à Pesquisa do Estado de Minas Gerais (FAPEMIG) for supporting this work (APQ-00544-23, APQ-05218-23). M. V. M. gratefully acknowledges the financial support from FAPEMIG and CNPq Foundations, Brazil, through a research productivity fellowship (BPQ-APQ06579-24). L. D. G. B. thanks FAPEMIG for the master's fellowship. W. C. N. thanks FAPERJ (projects E-26/010.000978/2019 and E-26/010.1553/2019). G. P. G. thanks FAPERJ (project E-26/201.314/2022) and CNPq (project 307135/2023-3). M. V. M. and L. D. G. B. thank (PIBIC/PIBITI_CNPq, PIBICT_FAPEMIG, PRPPG-UNIFAL-MG). The authors thank

PROAP and PRPPG (UNIFAL-MG) and the laboratories of UNIFAL-MG (IR spectroscopy, TG/DSC analysis- Edital FAPEMIG 03/2023, Powder XRD Multiuser Laboratory (LabcrystAL)), SCXRD diffraction facilities (UFF) and magnetic measurements (UFRJ). The authors acknowledge the use of the Lobo Carneiro supercomputer at the Núcleo Avançado de Computação de Alto Desempenho (NACAD) for carrying out the theoretical calculations, under Project ID a20006. The authors would also like to thank the National Laboratory for Scientific Computing (LNCC/MCTI, Brazil) for providing HPC resources on the SDumont supercomputer, which contributed to the research results reported in this paper (URL: http://sdumont.lncc.br).

References

1 N. Ishikawa, M. Sugita, T. Ishikawa, S. Y. Koshihara and Y. Kaizu, *J. Am. Chem. Soc.*, 2003, **125**(29), 8694–8695.
2 J. D. Rinehart and J. R. Long, *Chem. Sci.*, 2011, **2**(11), 2078.
3 W. H. Harman, T. D. Harris, D. E. Freedman, H. Fong, A. Chang, J. D. Rinehart, A. Ozarowski, M. T. Sougrati, F. Gradjean, G. J. Long, J. R. Long and C. J. Chang, *J. Am. Chem. Soc.*, 2010, **132**(51), 18115–18126.
4 J. M. Frost, K. L. M. Harriman and M. Murugesu, *Chem. Sci.*, 2016, **7**(4), 2470–2491.
5 A. E. Ion, S. Nica, A. M. Madalan, S. Shova, J. Valleko, M. Julve, F. Lloret and M. Andruh, *Inorg. Chem.*, 2015, **54**(1), 16–18.
6 Y. Cui, Y. Xu, X. Liu, Y. Li, B. Wang, Y. Dong, W. Li and S. Lei, *Chem. – Asian J.*, 2019, **14**(15), 2620–2628.
7 S. C. Manna, S. Mistri and E. Zangrando, *Inorg. Chim. Acta*, 2014, **413**, 166–173.
8 N. de la Pinta, A. B. Caballero, G. Madariaga, J. M. Ezpeleta, A. Rodríguez-Diéguez, J. M. Salas and R. Cortés, *CrystEngComm*, 2014, **16**(36), 8322–8326.
9 L. Shi, F.-X. Shen, D. Shao, Y.-Q. Zhang and X.-Y. Wang, *CrystEngComm*, 2019, **21**(20), 3176–3185.
10 N. V. Reis, M. V. Marinho, T. R. G. Simões, K. C. Metz, R. C. A. Vaz, W. X. C. Oliveira, C. L. M. Pereira, W. P. Barros, C. B. Pinheiro, S. O. K. Giese, D. L. Hughes, K. R. Pirota, W. C. Nunes and H. O. Stumpf, *Polyhedron*, 2019, **171**(2), 203–211.
11 (*a*) L. D. S. Mariano, I. M. L. Rosa, N. R. de Campos, A. C. Doriguetto, D. F. Dias, W. D. do Pim, A. K. S. M. Valdo, F. T. Martins, M. A. Ribeiro, E. E. B. de Paula, E. F. Pedroso, H. O. Stumpf, J. Cano, F. Lloret, M. Julve and M. V. Marinho, *Cryst. Growth Des.*, 2020, **20**(4), 2462–2476; (*b*) N. R. de Campos, C. A. Simosono, I. M. Landre Rosa, R. M. R. da Silva, A. C. Doriguetto, W. D. do Pim, T. R. Gomes Simões, A. K. S. M. Valdo, F. T. Martins, C. V. Sarmiento, W. C. Nunes, G. P. Guedes, E. F. Pedroso, C. L. M. Pereira, H. O. Stumpf, F. Lloret, M. Julve and M. V. Marinho, *Dalton Trans.*, 2021, **50**(31), 10707–10728; (*c*) T. T. da Cunha, V. M. M. Barbosa, W. X. C. Oliveira, E. F. Pedroso, D. M. A. García, W. C. Nunes and C. L. M. Pereira, *Inorg. Chem.*, 2020, **59**(18), 12983–12987; (*d*) C. A. Simosono, L. S. Flores, T. R. G. Simões, W. D. do Pim, M. Julve and M. V. Marinho, *CrystEngComm*, 2024, **27**(2), 176–183; (*e*) T. R. G. Simões, W. D. do Pim, I. F. Silva, W. X. C. Oliveira, C. B. Pinheiro, C. L. M. Pereira, F. Lloret, M. Julve and H. O. Stumpf, *CrystEngComm*, 2013, **15**(47), 10165–10170; (*f*) L. Lisnard, L.-M. Chamoreau, Y. Li and Y. Journaux, *Cryst. Growth Des.*, 2012, **12**(10), 4955–4962.
12 (*a*) C. L. M. Pereira, E. F. Pedroso, H. O. Stumpf, M. A. Novak, L. Ricard, R. Ruiz-García, E. Rivière and Y. Journaux, *Angew. Chem., Int. Ed.*, 2004, **43**(8), 956–958; (*b*) E. Pardo, D. Cangussu, M. Dul, R. Lescouëzec, P. Herson, Y. Journaux, E. F. Pedroso, C. L. M. Pereira, M. C. Muñoz, R. Ruiz-García, J. Cano, P. Amorós, M. Julve and F. Lloret, *Angew. Chem., Int. Ed.*, 2008, **47**(22), 4211–4216; (*c*) I. Fernández, R. Ruiz, J. Faus, M. Julve, F. Lloret, J. Cano, X. Ottenwaelder, Y. Journaux and M. C. Muñoz, *Angew. Chem., Int. Ed.*, 2001, **40**(16), 3039–3042; (*d*) J. Ferrando-Soria, R. Ruiz-García, J. Cano, S. Stiriba, J. Vallejo, I. Castro, M. Julve, F. Lloret, P. Amorós, J. Pasán, C. Ruiz-Pérez, Y. Journaux and E. Pardo, *Chem. – Eur. J.*, 2012, **18**(6), 1608–1617; (*e*) M.-C. Dul, R. Lescouëzec, L.-M. Chamoreau, Y. Journaux, R. Carrasco, M. Castellano, R. Ruiz-García, J. Cano, F. Lloret, M. Julve, C. Ruiz-Pérez, O. Fabelo and E. Pardo, *CrystEngComm*, 2012, **14**(17), 5639; (*f*) W. X. C. Oliveira, M. A. Ribeiro, C. B. Pinheiro, M. M. da Costa, A. P. S. Fontes, W. C. Nunes, D. Cangussu, M. Julve, H. O. Stumpf and C. L. M. Pereira, *Cryst. Growth Des.*, 2015, **15**(3), 1325–1335; (*g*) J. E. Francescon, S. C. de J. Pfau, K. W. Borth, M. V. Marinho, E. F. Pedroso, S. O. K. Giese, C. L. M. Pereira, A. J. F. Miorim, G. M. Maciel, D. L. Hughes, J. Cano, M. Julve, H. O. Stumpf and T. R. G. Simões, *J. Mol. Struct.*, 2025, **1328**, 141272.
13 F. Nesse, *Wiley Interdiscip. Rev.:Comput. Mol. Sci.*, 2025, **15**, e70019.
14 F. Weigend and R. Ahlrichs, *Phys. Chem. Chem. Phys.*, 2005, **7**(18), 3297.
15 C. Kollmar, K. Sivalingam, Y. Guo and F. Neese, *J. Chem. Phys.*, 2021, **155**, 234104.
16 L. F. Chibotaru and L. Ungur, *J. Chem. Phys.*, 2012, **137**(6), 064112.
17 Bruker, *APEX4, SAINT and SADABS*, Bruker AXS Inc., Madison, Wisconsin, USA, 2021.
18 L. Krause, R. Herbst-Irmer, G. M. Sheldrick and D. Stalke, *J. Appl. Crystallogr.*, 2015, **48**(1), 3–10.
19 G. M. Sheldrick, *Acta Crystallogr., Sect. C:Struct. Chem.*, 2015, **71**(1), 3–8.
20 C. F. Macrae, P. R. Edgington, P. McCabe, E. Pidcock, G. P. Shields, R. Taylor, M. Towler and J. van de Streek, *J. Appl. Crystallogr.*, 2006, **39**(3), 453–457.
21 B. Ugale, D. Singh and C. M. Nagaraja, *J. Solid State Chem.*, 2015, **226**, 273–278.
22 C. A. Simosono, R. M. R. da Silva, N. R. de Campos, M. A. R. Silva, A. C. Doriguetto, L. S. Flores, C. C. Correa, T. R. G. Simões, A. K. S. M. Valdo, F. T. Martins, F. Garcia, G. P. Guedes, B. R. L. Galvão, J. Cancino-Bernardi, R. D. dos Reis, H. O. Stumpf, D. D. Justino, P. F. R. Ortega,

W. D. do Pim, M. Julve and M. V. Marinho, *Molecules*, 2023, **28**(5), 2086.
23 M. V. Marinho, L. D. C. Visentin, M. C. de Souza, R. Diniz, K. Krambrock, M. I. Yoshida and F. C. Machado, *Polyhedron*, 2010, **29**(13), 2657–2666.
24 V. M. Wallace, N. R. Dhumal, F. M. Zehentbauer, H. J. Kim and J. Kiefer, *J. Phys. Chem. B*, 2015, **119**(46), 14780–14789.
25 T. R. G. Simões, M. V. Marinho, J. Pasán, H. O. Stumpf, N. Moliner, F. Lloret and M. Julve, *Dalton Trans.*, 2019, **48**(27), 10260–10274.
26 M. V. Marinho, T. R. G. Simões, M. A. Ribeiro, C. L. M. Pereira, F. C. Machado, C. B. Pinheiro, H. O. Stumpf, J. Cano, F. Lloret and M. Julve, *Inorg. Chem.*, 2013, **52**(15), 8812–8819.
27 T. R. G. Simões, R. V. Mambrini, D. O. Reis, M. V. Marinho, M. A. Ribeiro, C. B. Pinheiro, J. Ferrando-Soria, M. Déniz, C. Ruiz-Pérez, D. Cangussu, H. O. Stumpf, F. Lloret and M. Julve, *Dalton Trans.*, 2013, **42**(16), 5778–5795.
28 M. Llunell, D. Casanova, J. Cirera, P. Alemany, and S. Alvarez, *SHAPE: Program for the Stereochemical Analysis of Molecular Fragments by Means of Continuous Shape Measures and Associated Tools, v2.1, Eletronic Structure Group*, Universitat de Barcelona, 2013.
29 J. G. Wang, J. H. Qin, L. Li and L. F. Ma, *Synth. React. Inorg., Met.-Org., Nano-Met. Chem.*, 2014, **44**(1), 112–117.
30 J. H. Qin, S. J. Liu and H. R. Wang, *Synth. React. Inorg., Met.-Org., Nano-Met. Chem.*, 2015, **45**(1), 68–73.
31 Y. Zhao, L. L. Dang, Z. M. Zhai, L. F. Ma and L. Y. Wang, *J. Solid State Chem.*, 2020, **290**, 121573.
32 N. F. Chilton, R. P. Anderson, L. D. Turner, A. Soncini and K. S. Murray, *J. Comput. Chem.*, 2013, **34**(13), 1164–1175.
33 W. J. Tang, S. T. Wu, X. M. Bu, H. Y. Zhang, X. Q. Wei and D. Shao, *Polyhedron*, 2023, **229**, 116175.
34 A. K. Mondal, S. Khatua, K. Tomar and S. Konar, *Eur. J. Inorg. Chem.*, 2016, **2016**(22), 3545–3552.
35 X. Liu, L. Sun, H. Zhou, P. Cen, X. Jin, G. Xie, S. Chen and Q. Hu, *Inorg. Chem.*, 2015, **54**(18), 8884–8886.
36 L. Váhovská, O. Bukrynov, I. Potočňák, E. Čižmár, A. Kliuikov, S. Vitushkina, M. Dušek and R. Herchel, *Eur. J. Inorg. Chem.*, 2019, **2019**(2), 250–261.
37 X. F. Ma, Z. Wang, X. L. Chen, M. Kurmoo and M. H. Zeng, *Inorg. Chem.*, 2017, **56**(24), 15178–15186.
38 E. Zahradníková, R. Herchel, I. Šalitroš, I. Císařová and B. Drahoš, *Dalton Trans.*, 2020, **49**(26), 9057–9069.
39 H. H. Cui, Y. Q. Zhang, X. T. Chen, Z. Wang and Z. L. Xue, *Dalton Trans.*, 2019, **48**(28), 10743–10752.
40 R. Boča, C. Rajnák, J. Titiš and D. Valigura, *Inorg. Chem.*, 2017, **56**(3), 1478–1482.
41 D. Reta and N. F. Chilton, *Phys. Chem. Chem. Phys.*, 2019, **21**(42), 23567–23575.
42 K. S. Cole and R. H. Cole, *J. Chem. Phys.*, 1941, **9**(4), 341–351.
43 C. Rajnák, J. Titiš, R. Boča, A. Palii and E. Garlatti, *Magnetochemistry*, 2021, **7**, 76–111.
44 S. G. McAdams, A. M. Ariciu, A. K. Kostopoulos, J. P. S. Walsh and F. Tuna, *Coord. Chem. Rev.*, 2017, **345**, 216–239.
45 A. I. Costa, R. M. R. da Silva, L. D. G. Botelho, S. F. N. Coelho, F. A. Sigoli, J. Honorato, J. Ellena, F. T. Martins, A. M. Gomes, W. C. Nunes, F. Lloret, M. Julve and M. V. Marinho, *Dalton Trans.*, 2024, **53**, 3994–4004.
46 J. M. Zadrozny and J. R. Long, *J. Am. Chem. Soc.*, 2011, **133**(51), 20732–20734.
47 T. Jurca, A. Farghal, P. H. Lin, I. Korobkov, M. Murugesu and D. S. Richeson, *J. Am. Chem. Soc.*, 2011, **133**(40), 15814–15817.
48 (*a*) CCDC 2469011: Experimental Crystal Structure Determination, 2025, DOI: 10.5517/ccdc.csd.cc2nw6j9; (*b*) CCDC 2469012: Experimental Crystal Structure Determination, 2025, DOI: 10.5517/ccdc.csd.cc2nw6kb.